geosciences

MDPI

Article

Discrete Element Simulation on the Evolution Mechanism of Excavation Damage Zone in Deep-Buried Tunnels Under Confining Pressure and Comprehensive Structural Planes

Zhina Liu [1,*], Yan Qiao [2], Yuanfeng Suo [1] and Haoyu Diao [2]

[1] College of Geosciences, China University of Petroleum-Beijing, Beijing 102249, China; suoyuanfeng@gmail.com
[2] Downhole Operation Research Department, CNPC Engineering Technology R&D Company Limited, Beijing 102206, China; qiaoyandri@cnpc.com.cn (Y.Q.)
* Correspondence: zhina.liu@cup.edu.cn

Abstract

The failure mechanism of fractured rock masses under high in situ stress is crucial to the stability of deep underground engineering. This study employs the discrete element method to investigate the evolution of the excavation damage zone (EDZ) in deep-buried tunnels. Numerical models of granite were developed to analyze how confining pressure influences single fractures with varying characteristics and to compare the behavior of filled versus unfilled fractures in double-fracture configurations. The results show the following: (1) confining pressure exerts a dual role, promoting crack initiation and EDZ expansion in intact rock and exposed fractures due to stress concentration while suppressing damage near hidden filled fractures through confinement; (2) EDZ geometry is governed by fracture orientation and filling condition, with filled fractures maintaining stress continuity and raising the crack initiation stress ratio to 0.3–0.4; (3) in multi-fracture setups, unfilled fractures facilitate stress release and crack coalescence, whereas filled fractures act as barriers, diverting cracks and promoting symmetric stress redistribution; and (4) models accurately reproduced failure patterns from real rockburst cases, validating the method for predicting fracture behavior, with filled fractures reducing EDZ area by up to 44%. These findings provide theoretical support for rockburst risk assessment and support design in complex geological conditions.

Keywords: excavation damage zone; confining pressure; discrete element simulation; rockburst; stress distribution

Academic Editor: Xiangchao Shi

Received: 28 October 2025
Revised: 19 November 2025
Accepted: 20 November 2025
Published: 21 November 2025

Citation: Liu, Z.; Qiao, Y.; Suo, Y.; Diao, H. Discrete Element Simulation on the Evolution Mechanism of Excavation Damage Zone in Deep-Buried Tunnels Under Confining Pressure and Comprehensive Structural Planes. *Geosciences* **2025**, *15*, 443. https://doi.org/10.3390/geosciences15120443

1. Introduction

With the rapid development of underground engineering toward greater depths, the issue of rock mass stability under high in situ stress conditions has become increasingly prominent. The stability of deep underground excavations remains a critical challenge in rock engineering, particularly in complex geological conditions involving high in situ stresses and pre-existing discontinuities [1,2]. The formation and evolution of excavation damage zones (EDZ) around underground openings have attracted significant research attention due to their substantial implications for engineering safety and long-term stability [3,4]

Extensive investigations have been conducted to understand the failure mechanisms surrounding underground excavations. Laboratory experiments and field observations have revealed that the development of EDZ is intrinsically influenced by the interaction between excavation-induced stress redistribution and pre-existing geological structures [5–7]. Particularly in deep tunnels, the presence of structural planes significantly alters stress distribution patterns and failure characteristics, often leading to complex damage evolution pattens and potential rockburst hazards [8–10]. Recent advances in monitoring techniques, such as non-linear ultrasonic methods, have provided new insights into damage progression in rock masses [11].

The role of natural fractures in the damage evolution process has been increasingly recognized. Zhao et al. (2020) demonstrated that joint surface roughness and orientational anisotropy substantially affect EDZ characteristics [12], while Lei et al. (2017) emphasized the importance of natural fractures in controlling damage progression [13]. Recent studies have further highlighted the significance of infilled fractures in modifying rock mass behavior. Indraratna et al. (2010, 2014) systematically investigated the effect of soil-infilled joints on stability [14,15], revealing that filling materials significantly alter the shear strength characteristics of rock discontinuities. The evolution of stress-induced borehole breakouts in anisotropic rocks has been effectively analyzed using discrete element modeling [16], while three-dimensional DEM simulations have provided new perspectives on V-shaped borehole breakouts [17].

Field studies from major projects have contributed valuable empirical data. Hao et al. (2016) analyzed EDZ development in columnar jointed rock masses at the Baihetan diversion tunnel [18], demonstrating the critical influence of rock mass structure on damage zone characteristics. Similarly, advanced numerical methods incorporating digital image processing have enabled more accurate correlations between mineral composition and mechanical properties [19], enhancing our understanding of rock mass behavior at the micro-scale.

Despite these advances, the understanding of how filled fractures influence EDZ development under high-stress conditions remains incomplete. Previous research has primarily focused on either intact rock masses or unfilled discontinuities, with limited attention to the coupled effects of fracture filling conditions and confining pressure [20,21]. Furthermore, recent research has advanced our understanding of the mechanical behavior of rock materials under confining pressure unloading paths [22–24] and has provided new methodologies for microseismic source location in cavern-containing rock masses [25], continuum analysis of structurally controlled displacements for large-scale underground caverns [26], and displacement back-analysis of rock mass parameters using intelligent optimization methods [27]. These studies have deepened the understanding of the mechanical behavior of surrounding rock and stability assessment in complex geological environments.

This study aims to address these research gaps through discrete element modeling of granite specimens containing both single and multiple filled fractures. By examining the controlling effects of fracture geometry, spatial position, and filling conditions on EDZ development, this research seeks to establish a comprehensive understanding of the failure mechanisms in fractured rock masses under high in situ stress conditions. The findings are expected to provide valuable insights for stability assessment and support design in deep underground engineering projects.

2. Method and Model Setup

2.1. Numerical Simulation Method

This study employs the Particle Flow Code (PFC2D 5.0), a discrete element method-based numerical approach, to simulate the mechanical behavior of heterogeneous geological materials [28]. In this framework, the rock mass is represented as an assembly of densely packed circular particles. The Linear Parallel Bond Model (LPBM) was adopted

as the contact model. This model was selected for its capacity to accurately capture the full range of mechanical response of hard, brittle rocks, like granite, from linear elastic deformation to macroscopic brittle fracture. The LPBM effectively reproduces the initiation, propagation, and coalescence of microcracks under various stress conditions, which is essential for realistically modeling excavation-induced damage zoning and the associated acoustic emission events, which is the primary focus of this study.

The model incorporates a combined failure criterion that integrates the Mohr–Coulomb shear strength theory with the maximum tensile stress criterion, allowing it to represent multiple failure mechanisms, including tensile cracking and shear slip [29]. When the stress between bonded particles exceeds either the shear or tensile strength threshold, the bond fails, resulting in a reduction in local stiffness and strength. This micro-level mechanism manifests macroscopically as crack initiation and growth. As a result, the adopted modeling approach successfully captures the progressive accumulation of damage and the evolution of failure in rock materials under mechanical loading.

2.2. Model Setup

2.2.1. Models Containing a Single Pre-Existing Fracture

To systematically investigate the influence of confining pressure on rock fracture behavior, this study developed five discrete element models, each containing a single pre-existing fracture (designated as Models A, D, D′, H, and H′). Model A represents an intact rock mass without any pre-existing fracture, serving as the benchmark. The other four models all contain pre-existing fractures with a consistent dip of 60°, but differ in geometric and mechanical properties, including spatial location, relationship to the borehole (exposed or hidden), and infill condition (filled or unfilled), thereby establishing a basis for comparative analysis (Table 1). All models maintain consistent geometric dimensions and initial fracture lengths, with the only variable parameter being the lateral confining pressure ($\sigma_2 = \sigma_3$), enabling analysis of the confining pressure effect.

Table 1. Models containing a single pre-existing fracture.

Models	Fracture Characteristics			
	Inclinations	Above/Below the Horizontal Axis	Exposed/Hidden to the Borehole	Filled/ Unfilled
Model A	No fractures			
Model D	60°	Above	Exposed	Filled
Model D′	60°	Above	Exposed	Unfilled
Model H	60°	Below	Hidden	Filled
Model H′	60°	Below	Hidden	Unfilled

The specific characteristics of each model are as follows: Model D features a filled fracture exposed to the borehole boundary; Model D′ contains an unfilled fracture at the identical location; Model H contains a filled fracture embedded within the rock mass and located below the horizontal axis; and Model H′ contains an unfilled fracture at the same embedded location (Table 1; Figure 1a–c). By systematically varying the confining pressure (set to 6 MPa, 12 MPa, and 18 MPa, respectively), this study focuses on examining the coupling effect of confining pressure and fracture attributes on the geometry of the excavation damage zone, stress distribution characteristics, and crack propagation patterns.

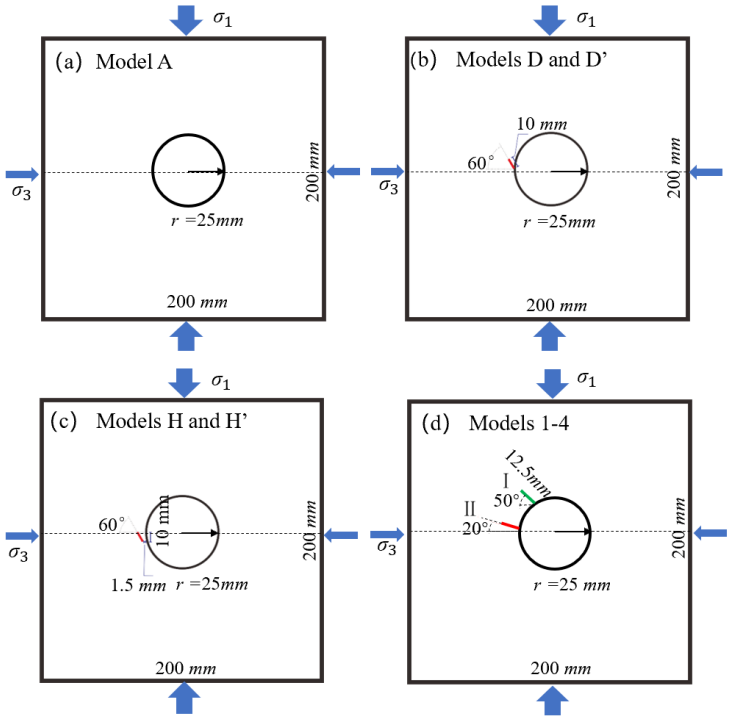

Figure 1. Diagram of numerical models: (**a**) homogeneous model A, (**b**) Models D and D' containing a single fracture that is exposed to boreholes, (**c**) Models H and H' containing a single fracture that is not exposed to boreholes, and (**d**) Models 1–4 containing two fractures.

2.2.2. Models Containing Two Pre-Existing Fractures

To further investigate the interaction between multiple geological structures and their combined effect on excavation damage, discrete element models containing two pre-existing fractures were established (Figure 1d). Building upon the methodology for single fracture models, four distinct scenarios were configured to systematically analyze the influence of fracture infill conditions (Table 2). This setup enables a comprehensive examination of how different filling states control surrounding rock stability, with particular focus on crack interaction, stress redistribution between adjacent fractures, and the resulting failure mechanisms in multi-fracture rock masses.

Table 2. Models containing two pre-existing fractures.

Models	Fracture I	Fracture II	Simulated Case	Remarks
Model 1	No filling	No filling	Actual working condition	Benchmark model
Model 2	Filled	No filling	Contrast working condition	Single side filling
Model 3	No filling	Filled	Contrast working condition	Single side filling
Model 4	Filled	Filled	Contrast working condition	Full filling

2.3. Numerical Models

The numerical models were constructed with dimensions of 200 mm × 200 mm and a central borehole 50 mm in diameter. Each model consisted of approximately 40,000 discrete particles with radii ranging from 0.4 to 0.6 mm, effectively capturing the meso-scale structure of granite, which required several hours to complete on a standard workstation. The loading path followed the experimental procedure, beginning with an isotropic stress of 12 MPa applied, equal to the confining pressure in the x-direction and axial stress in the y-direction. The axial stress was then progressively increased until the excavation damage zone fully developed, while the confining pressure was maintained constant throughout the simulation via a servo-control mechanism.

Model calibration was performed through comparison with physical experiments conducted by Su et al. (2023) [21], which employed a true triaxial testing system at Guangxi University to perform biaxial compression tests on Beishan granite specimens containing circular boreholes and artificial, filled fractures. The granite composition comprises 54% potassium feldspar, 30% quartz, 10% plagioclase, and 4% biotite. Baseline mechanical parameters for the granite, listed in Table 3, were directly established through unconfined compression tests and Brazilian disk splitting tests. These directly measured parameters served as the essential reference data for calibrating the micro-mechanical properties in the discrete element models, ensuring that the numerical response matched the physical benchmark tests.

Table 3. Microscopic mechanical parameters of discrete element models.

Parameters	Granite	Veins (Filled Fractures)	Rock–Vein Interface
Elastic modulus (GPa)	27	10	1
Normal/tangential stiffness ratio	3	2.5	2.5
Tensile strength (MPa)	123 ± 12.3	30 ± 3	0.5
Cohesion (MPa)	133 ± 13.3	35 ± 3.5	1
Internal friction angle (°)	20	15	15

2.4. Monitoring Scheme and Data Processing

To comprehensively monitor the evolution of the excavation damage zone, a systematic monitoring scheme was implemented in the discrete element models. Three sets of 10 mm diameter stress measurement circles were installed to track the stress state within the rock specimens (Figure 2). These consisted of two horizontal sets, each containing ten circles spaced 5 mm apart along the left and right walls of the borehole (Figure 2a,c), and one circumferential set with thirty-six circles arranged at 10° intervals around the borehole perimeter (Figure 2b). This layout enabled detailed comparison of the stress distribution patterns and supported interpretation of the differences in excavation damage zone geometries.

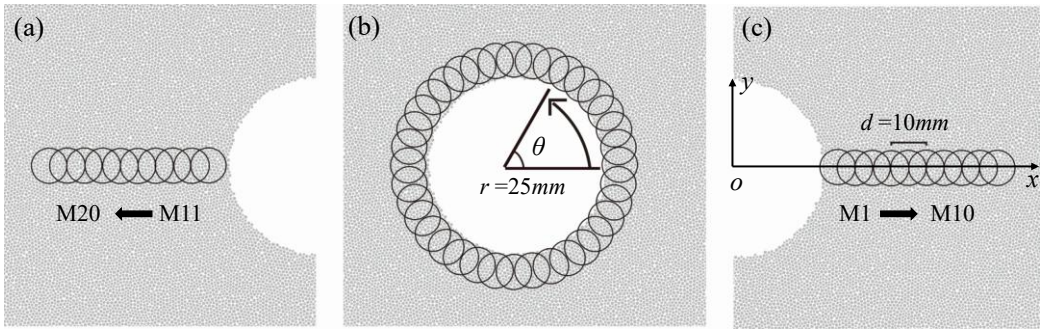

Figure 2. Three sets (**a**–**c**) of measurement circles in the particle-based DEM models of squared granite samples.

This stress distribution can be obtained from the stress measurement circles, including radial stress (σ_{rr}), tangential stress ($\sigma_{\theta\theta}$), and shear stress ($\tau_{r\theta}$). These three stresses can be expressed in the polar coordinate system as follows [30]:

$$\begin{aligned} \sigma_{rr} &= \sigma_x \cos^2\theta + \sigma_y \sin^2\theta + 2\tau_{xy}\sin\theta\cos\theta \\ \sigma_{\theta\theta} &= \sigma_x \sin^2\theta + \sigma_y \cos^2\theta - 2\tau_{xy}\sin\theta\cos\theta \\ \tau_{r\theta} &= (\sigma_y - \sigma_x)\sin\theta\cos\theta + \tau_{xy}(\cos^2\theta - \sin^2\theta) \end{aligned} \quad (1)$$

Here, σ_x, σ_y, and τ_{xy} are the stress components calculated from the measurement circles, and θ is the angle direction measured counterclockwise from the *x*-axis (Figure 2b).

In addition to the recorded stress in the particle-based discrete element models, the analytical stress solutions for radial stress (σ_{rr}'), tangential stress ($\sigma_{\theta\theta}'$), and shear stress ($\tau_{r\theta}'$) under standard conditions were also calculated. Thus, the stress distribution in the damage zone of the granite sample with filled fractures was analyzed as follows [16,17,20]:

$$\begin{aligned}\sigma_{rr}' &= \frac{1}{2}(\sigma_1+\sigma_3)\left(1-\frac{a^2}{r^2}\right)+\frac{1}{2}(\sigma_1-\sigma_3)\left(1-4\frac{a^2}{r^2}+3\frac{a^4}{r^4}\right)\cos 2\theta \\ \sigma_{\theta\theta}' &= \frac{1}{2}(\sigma_1+\sigma_3)\left(1+\frac{a^2}{r^2}\right)-\frac{1}{2}(\sigma_1-\sigma_3)\left(1+3\frac{a^4}{r^4}\right)\cos 2\theta \\ \tau_{r\theta}' &= -\frac{1}{2}(\sigma_1+\sigma_3)\left(1+\frac{a^2}{r^2}\right)\left(1+2\frac{a^2}{r^2}-3\frac{a^4}{r^4}\right)\sin 2\theta\end{aligned} \quad (2)$$

where a is the borehole radius and r is the radial distance from the borehole axis.

Acoustic emission (AE) monitoring, based on moment tensor theory, was conducted to track microcrack development by recording bond breakage events. The threshold for detecting an AE event was set to the release of any finite strain energy; that is, every single micro-fracture (bond breakage) was recorded regardless of its magnitude. Each AE event was characterized by location, released energy, and source mechanism. The resulting signals were then processed to calculate event rates and cumulative energy. A clustering algorithm was applied to classify the spatial–temporal evolution of damage features across different stages [31]. Furthermore, an automated algorithm identified macroscopic damage zones using crack density thresholds, with image processing techniques employed to define their boundaries and measure geometry. This methodology ensured an unbiased record of fracture activity and enhanced the accuracy and efficiency of data interpretation.

3. Model Results

3.1. Models Containing a Single Pre-Existing Fracture

Numerical simulations demonstrate that confining pressure (6, 12, and 18 MPa) significantly influences both the geometric characteristics and failure mechanisms of the excavation damage zone (EDZ) across all model configurations. The response varies substantially depending on fracture geometry and filling conditions, revealing complex interactions between pre-existing discontinuities and stress fields.

In the homogeneous model (model A) without pre-existing fractures, increasing confining pressure systematically promotes EDZ expansion with distinct geometric progression. As shown in Figure 3, failure width increases from 52.8° to 58.1°, normalized depth from 1.72 to 1.92, and damaged area from 380 mm² to 452 mm² as confining pressure rises from 6 to 18 MPa, establishing a clear positive correlation in intact rock. This trend is corroborated by the failure evolution patterns in Figure 4, which are characterized by accelerated crack propagation toward the lower left region and intensified wall spalling, the latter of which produced 35% more ejected fragments.

Stress analysis reveals the underlying mechanism of asymmetric damage formation (Figure 5). Under an axial stress of 80 MPa, the elevated confining pressure enhances shear stress concentration within the 280–310° sector of the borehole wall, where measured values reach 45 MPa, significantly exceeding the analytical solution of 28 MPa. Simultaneously, radial stresses along horizontal monitoring lines increase by 60–75%, compared to the theoretical values, confirming that intensified stress concentrations drive more extensive crack propagation. The tangential stress generally agrees well with the analytical solution in most regions (0–150° and 240–270°), while the radial stress is systematically higher than theoretical predictions across the model domain. A systematic deviation of

shear stress in the 270–330° range is identified as the key factor causing the downward shift in the damage zone.

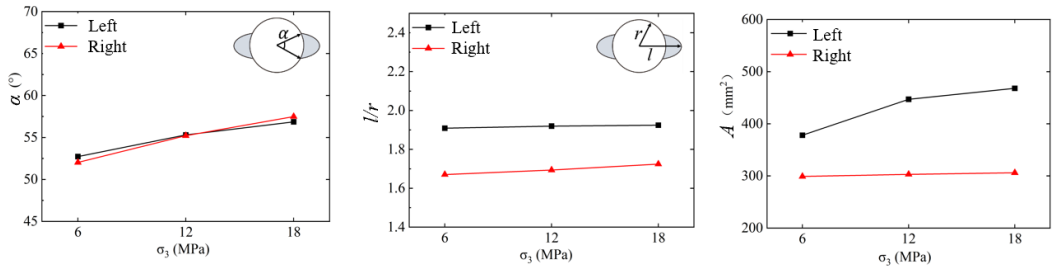

Figure 3. Comparison of geometric parameters of the damaged zone in model A under different confining pressures. Parameter A denotes the area of the damaged zone, as illustrated in the final column of Figure 4 at the failure stress state.

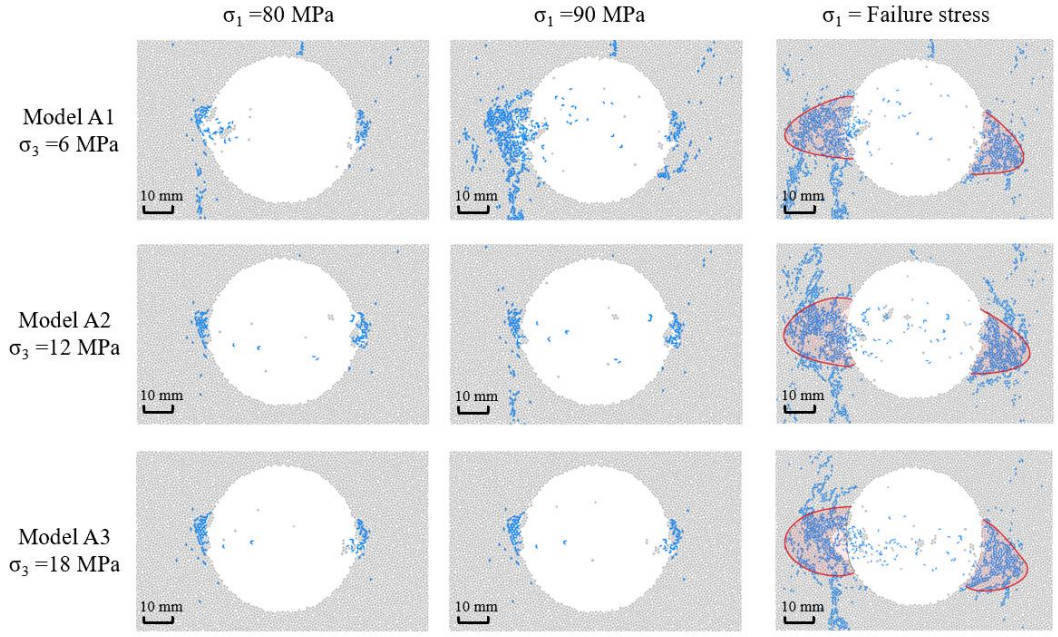

Figure 4. Simulation processes of model A under different confining pressures. The clusters of microcracks in the models are represented by blue dots, while the failure zones are delineated by red lines.

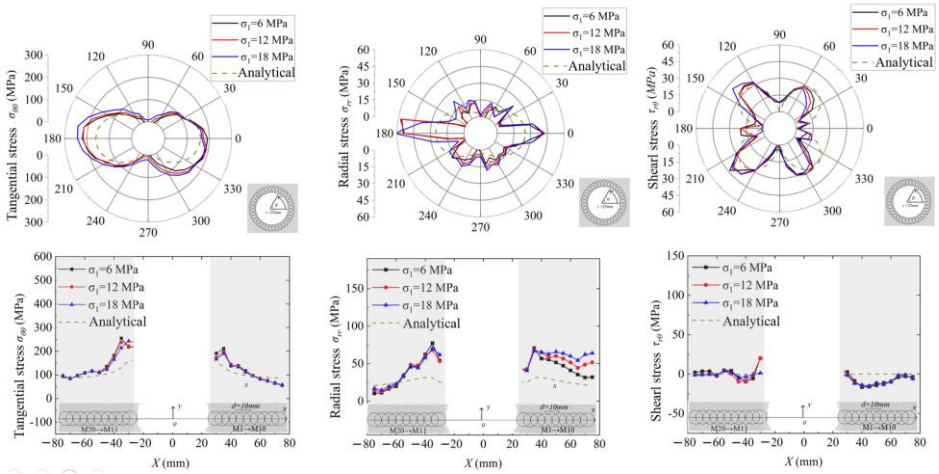

Figure 5. Stress distribution of model A under different confining pressures when the axial stress is 80 MPa.

The response of filled fracture models exhibits fundamental differences based on fracture exposure conditions. For exposed filled fractures (model D), a distinct positive correlation emerges between confining pressure and EDZ extent (Figure 6), with the damage width expanding from 38.4° to 49.2° and depth from 1.45 to 1.68 as the pressure increases. Under high confining pressure, cracks propagate upward from the left fracture tip at 55° while expanding more extensively on the right side, forming a 42% larger damage zone compared to in low-pressure conditions (Figure 7). Stress distributions at 90 MPa axial stress (Figure 8) show that elevated pressure shifts the left wall stress concentrations toward the 170–180° range, with radial stress peaks increasing from 38 MPa to 52 MPa, thereby steering the cracks upward. Furthermore, high-pressure models develop dual-stress-concentration loci on the right wall (near 15° and 330° with stresses of 48 MPa and 45 MPa, respectively), contrasting with the single locus (35 MPa) under lower pressure and explaining the expanded right side damage.

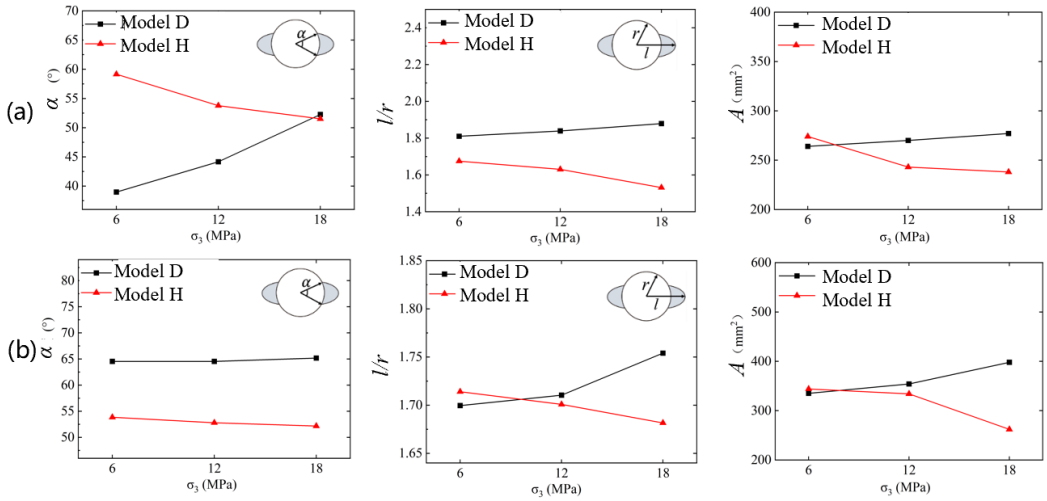

Figure 6. Comparison of geometric parameters of damage zones of Models D and H under different confining pressures: (**a**) the left damage zones; (**b**) the right damage zones. Parameter A denotes the area of the damaged zone, as illustrated in the final column of Figures 7 and 9 at the failure stress state.

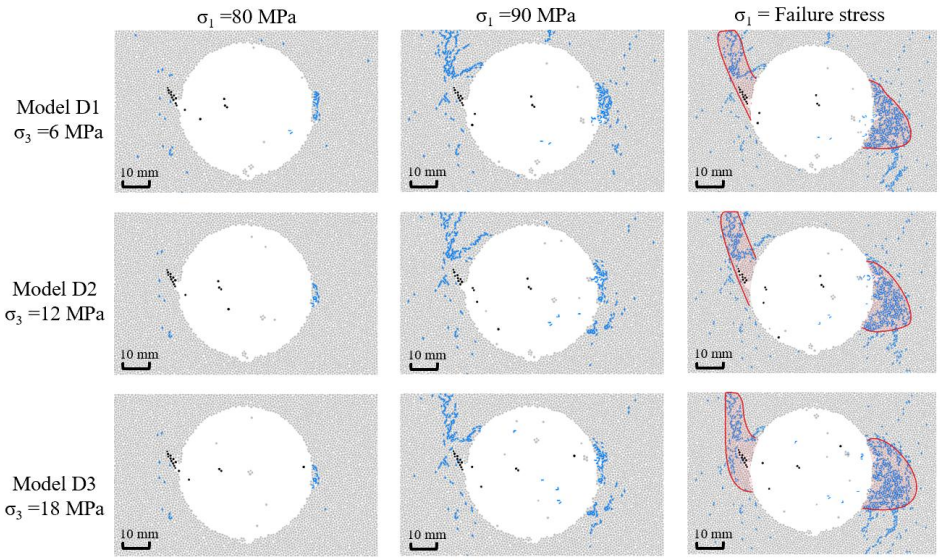

Figure 7. Simulation processes of Model D under different confining pressures. The clusters of microcracks in the models are represented by blue dots, while the failure zones are delineated by red lines.

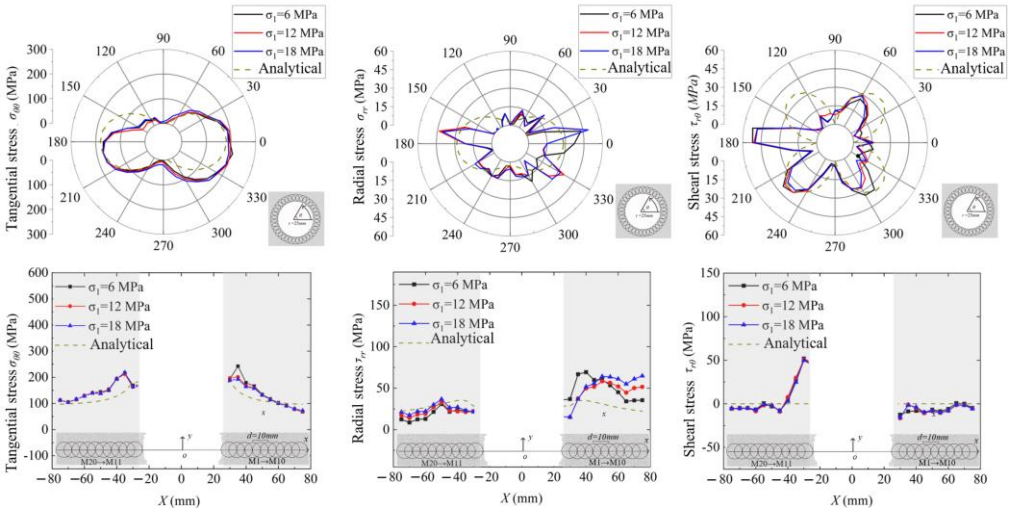

Figure 8. Stress distribution of Model D under different confining pressures when the axial stress is 90 MPa.

Conversely, hidden filled fractures (Model H) exhibit a negative correlation, with EDZ contraction under increasing confining pressure (Figure 6). The damage area decreases by 43% from low- to high-pressure conditions. The failure process (Figure 9) shows that at 80 MPa axial stress, the low-pressure model (H1) exhibits deep crack propagation with fractures extending 18.2 mm from the borehole wall, while the high-pressure model (H3) remains effectively suppressed with only 8.5 mm fracture propagation. Corresponding stress analysis (Figure 10) indicates significantly reduced hoop and radial stresses in Model H1, dropping to 40% and 35% of analytical solutions, respectively, indicating comprehensive stress release through microcracking. In contrast, higher confining pressures enhance rock mass confinement, increasing the crack initiation stress threshold by 28% and effectively inhibiting microcrack initiation, thereby restricting final damage development.

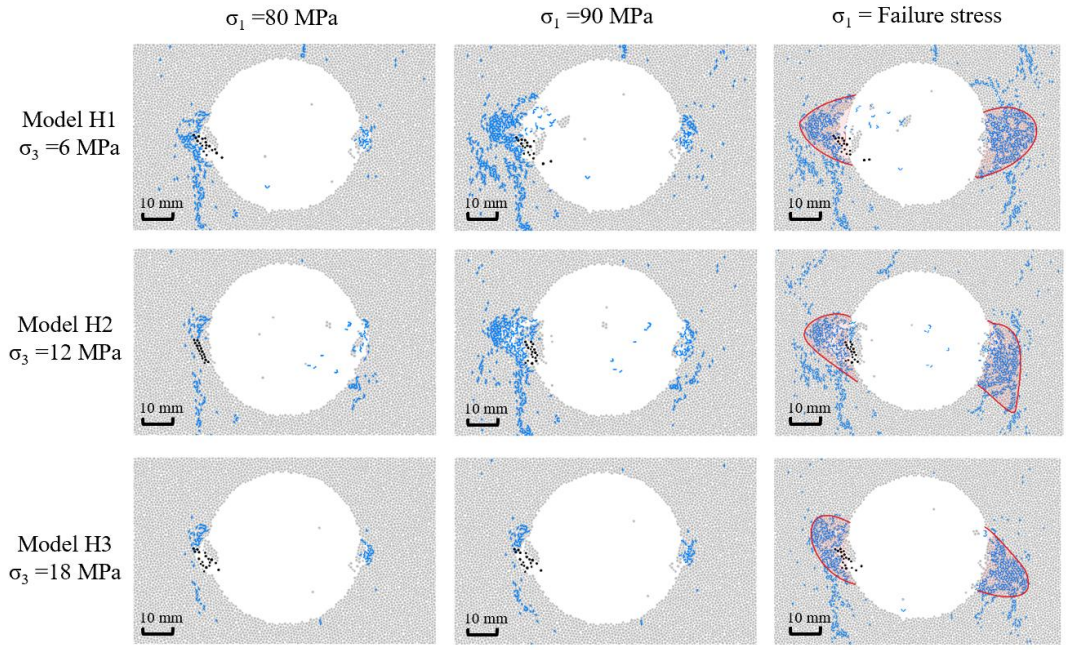

Figure 9. Simulation processes of Model H under different confining pressures. The clusters of microcracks in the models are represented by blue dots, while the failure zones are delineated by red lines.

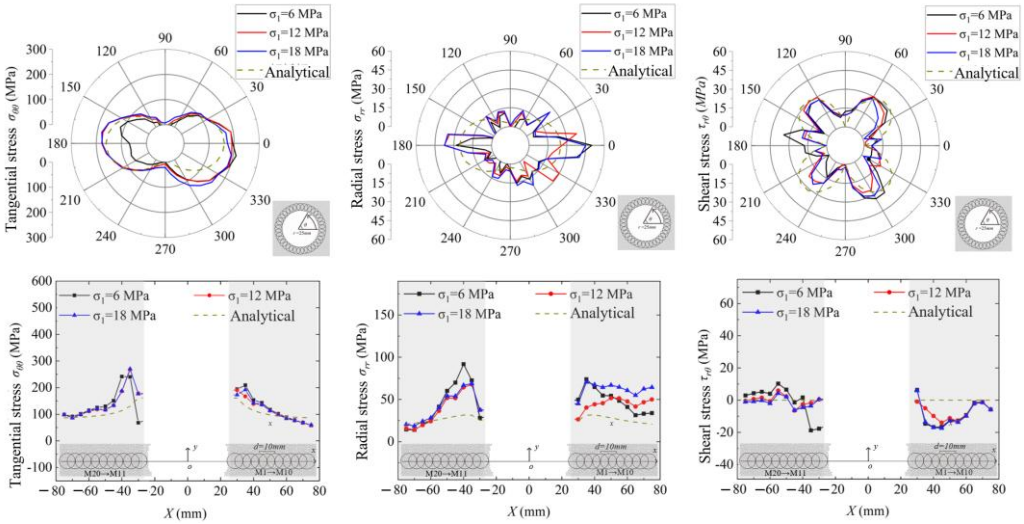

Figure 10. Stress distribution of Model H under different confining pressures when the axial stress is 80 MPa.

Unfilled fractures produce more pronounced and complex responses with heightened sensitivity to confining pressure. Exposed unfilled fractures (Model D′) maintain a strong positive correlation with confining pressure (Figure 11), developing the largest overall damage zones among all configurations. Although failure morphology resembles Model D (Figure 12), unfilled fractures show 25% greater pressure sensitivity in damage expansion rates. Stress analysis at 90 MPa (Figure 13) reveals that radial and shear stresses in high-pressure models (D′3) substantially exceed analytical predictions by 65–80%, accumulating critical strain energy that produces the largest ultimate damage zone with width reaching 61.3° and area expanding to 518 mm².

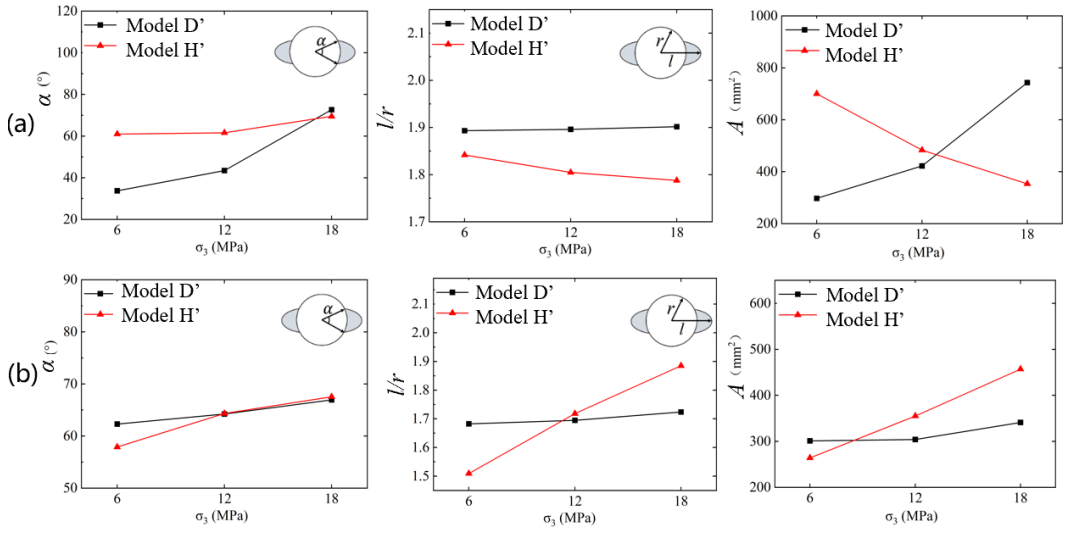

Figure 11. Comparison of geometric parameters of damage zones of Models D′ and H′ under different confining pressures: (**a**) the left damage zones; (**b**) the right damage zones. Parameter A denotes the area of the damaged zone, as illustrated in the final column of Figures 12 and 14 at the failure stress state.

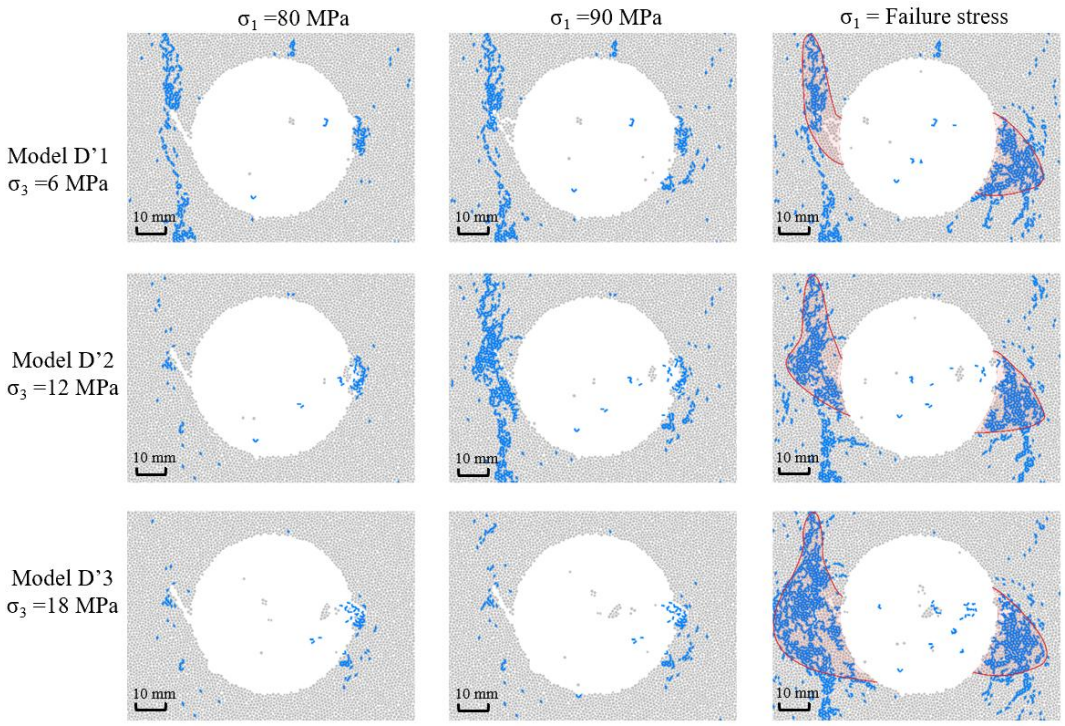

Figure 12. Simulation processes of Model D′ under different confining pressures. The clusters of microcracks in the models are represented by blue dots, while the failure zones are delineated by red lines.

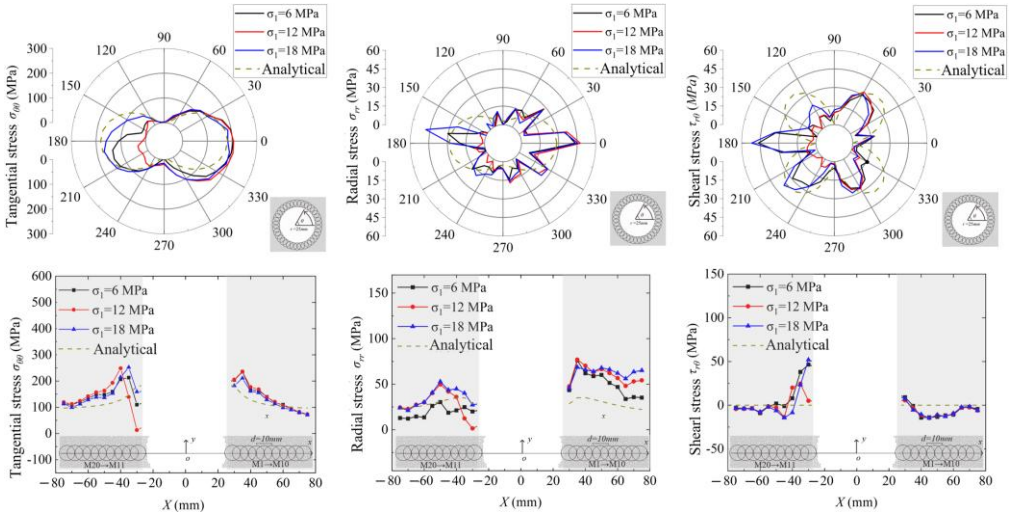

Figure 13. Stress distribution of Model D′ under different confining pressures when the axial stress is 90 MPa.

Hidden unfilled fractures (Model H′) display uniquely partitioned damage patterns (Figure 11), with the left-side damage area and depth decreasing by 32% and 28%, respectively, but right-side dimensions increasing by 41% and 37% with rising confining pressure. This pronounced asymmetry stems from early failure evolution: at 60 MPa axial stress, the low-pressure model (H′1) already shows crack propagation below the left fracture tip extending 12.4 mm into the rock mass (Figure 14), which is unobserved in high-pressure models. Corresponding stress distributions (Figure 15) show reduced hoop stress in Model H′1, decreasing to 55% of analytical solutions, indicating comprehensive left-side stress release. Consequently, stress concentration migrates to the right borehole wall, developing maximum hoop stress of 58 MPa near 300° in low-pressure models and

producing the most extensive right-side damage (width 46.8°) and largest total damaged area (489 mm²) among all single-fracture configurations.

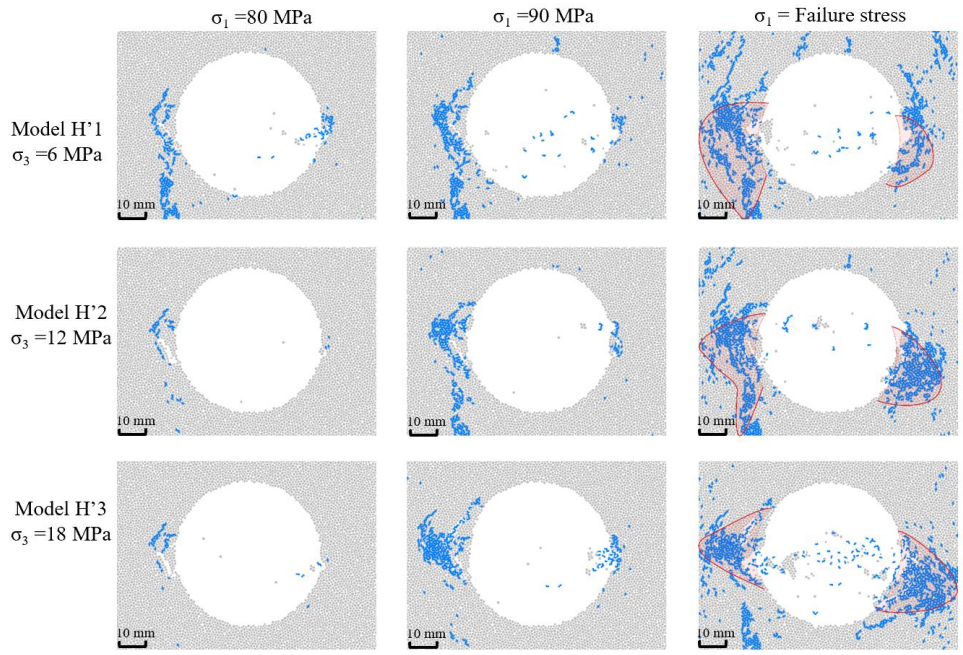

Figure 14. Simulation processes of Model H′ under different confining pressures. The clusters of microcracks in the models are represented by blue dots, while the failure zones are delineated by red lines.

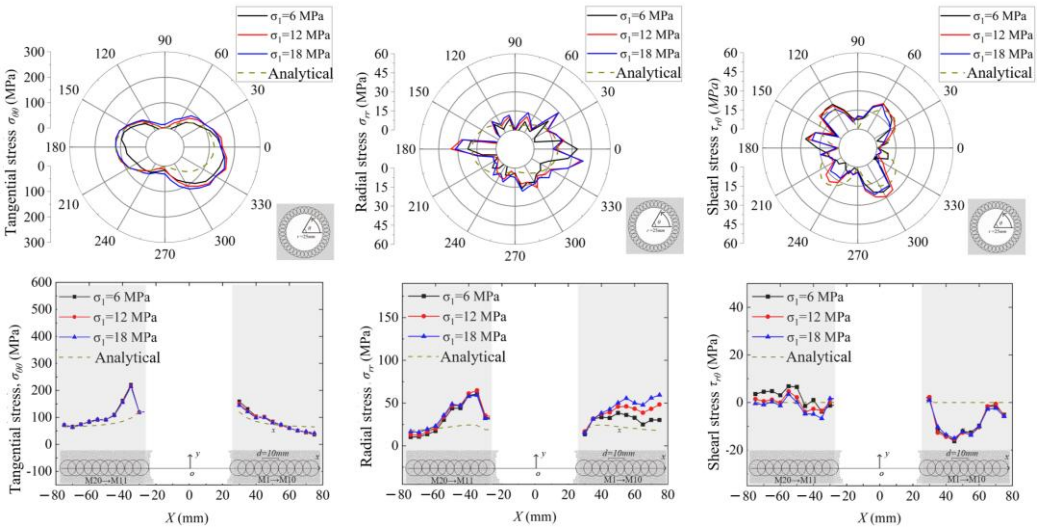

Figure 15. Stress distribution of Model H′ under different confining pressures when the axial stress is 60 MPa.

The characteristic stress analysis reveals that the crack initiation stress (σ_{cd}/σ_p) and crack damage stress (σ_{cd}/σ_p) ratios for fractured models fall within the lower bounds (0.3–0.4 and 0.6–0.8, respectively) proposed by Cai and Kaiser (2014), being significantly lower than the 0.5 and 0.9 ratios observed in intact rock [32], confirming that pre-existing fractures substantially reduce the stress thresholds required for damage initiation and propagation.

3.2. Models Containing Two Pre-Existing Fractures

Simulations of models with two pre-existing fractures under different filling conditions (models 1–4) reveal significant EDZ variations that highlight the critical role of fracture filling in rock mass stability. The comparative analysis demonstrates how filling materials alter fractures' mechanical properties and consequently affect damage evolution patterns around the excavation.

The filling state fundamentally governs EDZ geometry (Figure 16). Model 1 (both fractures unfilled) develops the most extensive damage zone with maximum width (65.2° on the left side, 58.7° on the right side), depth (normalized depth l/r = 2.15), and area (512 mm²). In contrast, model 4 (both fractures filled) exhibits minimal damage with reduced width (41.3° on left, 38.9° on right), depth (l/r = 1.62), and area (286 mm²). Models 2 (Fracture I filled) and 3 (Fracture II filled) show intermediate damage states. This progressive reduction in damage extent with increased fracture filling demonstrates that filling materials effectively suppress EDZ expansion by enhancing fracture strength and impeding crack propagation.

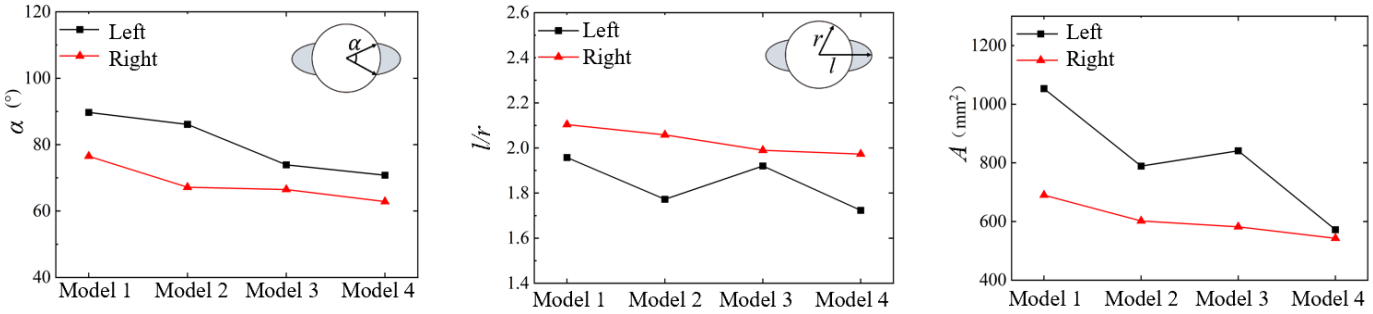

Figure 16. Comparison of geometric parameters of damage zones of models 1–4. Parameter A denotes the area of the damaged zone, as illustrated in the final column of Figure 17 at the failure stress state.

Failure processes (Figure 17) elucidate the underlying damage mechanisms. At 50 MPa axial stress, model 1 displays early crack coalescence between the two unfilled fractures, indicating low structural stability. Meanwhile, model 4 shows only localized spalling at fracture–borewall intersections. At 60 MPa axial stress, models 2–3 exhibit transitional behaviors: model 2 develops cracks upward from the tip of the unfilled Fracture I while the filled Fracture II remains intact, whereas model 3 forms cracks primarily between the two fractures with preferential propagation toward the unfilled one. By peak stress, model 1 forms a widespread, interconnected crack network with low density due to rapid stress release, while model 4 maintains optimal damage control with isolated microcracks that fail to coalesce into major failure planes.

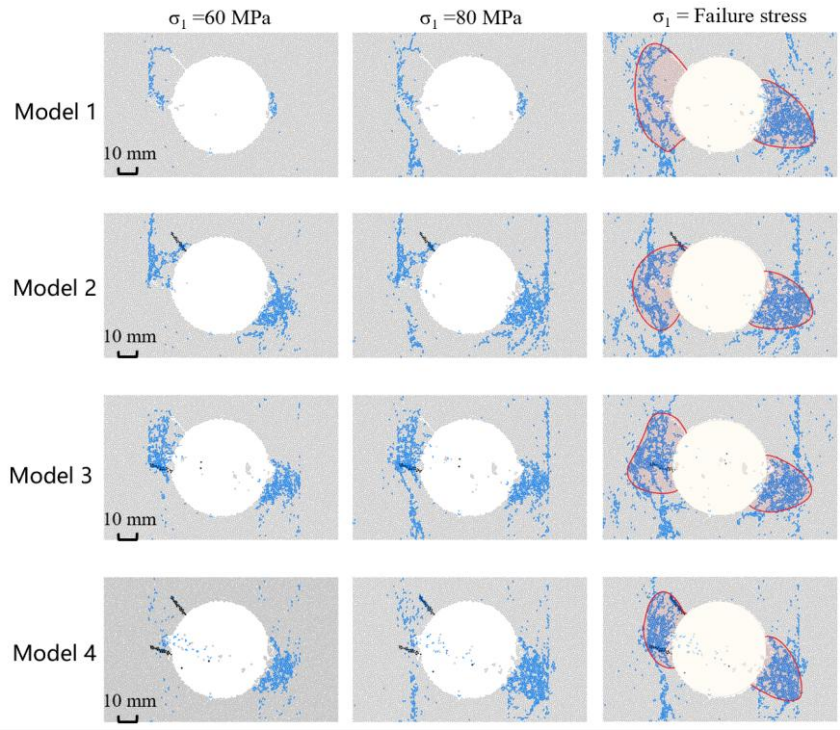

Figure 17. Simulation processes of models 1–4 containing two different pre-existing fractures. The clusters of microcracks in the models are represented by blue dots, while the failure zones are delineated by red lines.

Stress distributions (Figure 18) provide mechanical explanations for the observed damage patterns. At 60 MPa axial stress, models 1–3 show significant reductions (35–50%) in terms of hoop and radial stresses on the fractured left wall compared to analytical solutions, indicating substantial stress release through progressive failure. The unfilled fractures serve as stress relief points where stresses drop to near-zero values. In contrast, model 4 maintains high left-wall stresses exceeding analytical predictions by 15–20%, demonstrating that filling materials effectively transfer and sustain rock mass stress across fracture planes. This stress maintenance prevents the localized stress concentrations that typically initiate crack propagation, thereby inhibiting damage development.

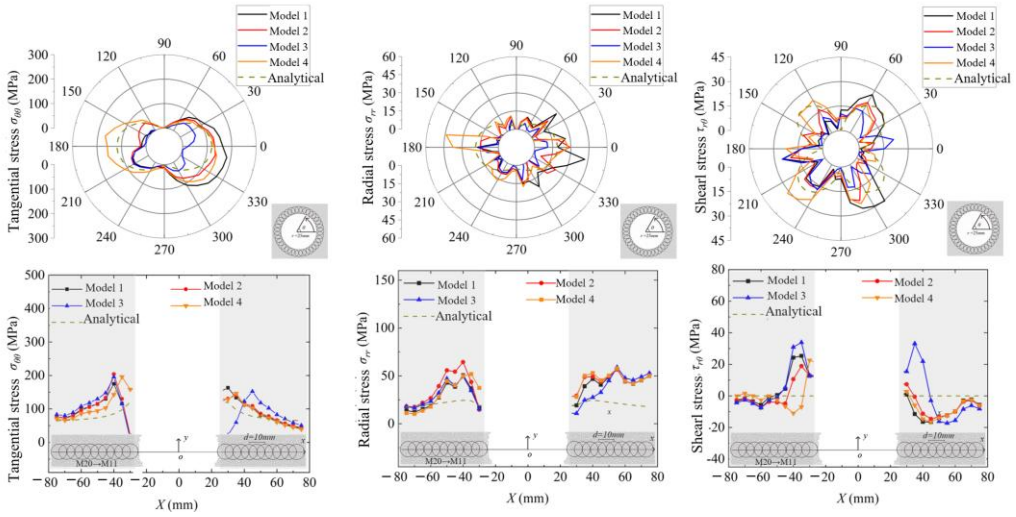

Figure 18. Stress distribution of models 1–4 when the axial stress is 60 MPa.

The simulation results further reveal that filling materials alter crack initiation sequences and propagation paths. In unfilled fracture models, cracks initiate simultaneously at multiple fracture tips and rapidly coalesce. In partially filled models, crack initiation preferentially occurs at the tips of unfilled fractures, with filled fractures acting as barriers that deflect crack paths. The filled fractures in models 2 and 3 reduce damage asymmetry by 42% and 28%, respectively, compared to model 1, confirming that fracture filling promotes more symmetric stress redistribution around excavations.

These findings validate that fracture filling significantly enhances excavation stability by maintaining stress continuity, increasing fracture strength, and preventing crack coalescence. The results provide critical insights for optimizing grouting strategies in fractured rock masses, particularly for underground projects where multiple intersecting fractures pose stability challenges.

4. Discussion

4.1. Influence of Confining Pressure

The numerical simulation results clearly demonstrate that confining pressure exerts a profoundly different influence on EDZ development depending on the presence and characteristics of pre-existing fractures. The observed responses can be attributed to the competing mechanisms of stress intensification and confinement-induced stabilization, with the specific fracture geometry and filling conditions determining which mechanism dominates.

In homogeneous rock (Model A) and models with exposed fractures (Models D and D′), a consistent positive correlation emerges between confining pressure and EDZ extent. This relationship stems primarily from stress intensification under increased differential stresses. Quantitative analysis reveals that in Model A, the damage width expanded from 52.8° to 58.1° and the damaged area increased from 380 mm^2 to 452 mm^2 as confining pressure rose from 6 to 18 MPa. The accelerated crack initiation, occurring at 74 MPa axial stress under high confinement compared to 82 MPa under low confinement, demonstrates how elevated pressure reduces the stress threshold for damage initiation. The mechanical basis for this behavior is evident in the stress distributions: under 80 MPa axial stress, shear stress concentration in the 280–310° sector reached 45 MPa under high confinement, markedly exceeding the 28 MPa analytical solution and driving more extensive crack propagation.

The response of filled fracture models reveals fundamental differences based on fracture orientation and exposure conditions. For exposed filled fractures (Model D), the dual stress concentration mechanism, with pressure-induced secondary stress concentration points developing at 15° and 330° on the right wall, explains the expanded damage zone under high confinement. The 42% larger damage zone under high-pressure conditions, coupled with the radial stress peaks increasing from 38 MPa to 52 MPa, demonstrates how exposed fractures serve as stress amplifiers under increasing confinement.

Conversely, hidden filled fractures (Model H) exhibit a distinctive negative correlation with confining pressure, with damage area decreasing by 43% from low- to high-pressure conditions. This confinement-induced stabilization operates through suppression of microcrack initiation and propagation. Under low confinement, the hidden fracture acts as a flaw where microcracks readily initiate, leading to comprehensive stress release as evidenced by the hoop and radial stresses dropping to 40% and 35% of analytical solutions, respectively. Higher confining pressures increase the crack initiation stress threshold by 28%, effectively inhibiting microcrack development and restricting final damage. This stabilization mechanism is particularly relevant for deep underground excavations where sealed, hidden fractures are common.

The most complex response emerges from hidden unfilled fractures (Model H′), which exhibit partitioned damage patterns with left-side damage decreasing by 32% while right-side damage increases by 41% with rising confining pressure. This asymmetry

results from the interplay between stress release on the fractured side and stress transfer to the intact side. At low confining pressure, the early activation of the left-side fracture leads to stress release (hoop stress reduced to 55% of analytical solutions) and consequent stress redistribution to the right borehole wall, where the maximum hoop stress of 58 MPa near 300° drives extensive right-side damage. Higher confining pressures mitigate this effect by stabilizing the fracture, resulting in more symmetric damage distribution.

The characteristic stress analysis provides crucial insights into the fundamental mechanics governing these responses. The significantly lower crack initiation stress (σ_{cd}/σ_p = 0.3–0.4) and crack damage stress (σ_{cd}/σ_p = 0.6–0.8) ratios for fractured models compared to intact rock (0.5 and 0.9, respectively) confirm that pre-existing fractures substantially reduce the stress thresholds required for damage initiation and propagation. This explains why fractured rock masses exhibit heightened sensitivity to confining pressure variations and why damage patterns evolve differently based on fracture characteristics.

These findings have profound implications for underground excavation design and stability assessment. The demonstrated dual role of confining pressure, both as a driver of stress intensification in certain geometries and as a stabilizer in others, underscores the necessity of comprehensive fracture characterization prior to excavation. Particularly critical is the identification of hidden unfilled fractures, which can trigger unexpected asymmetric failure patterns that conventional symmetrical analysis methods might overlook.

4.2. Influence of Composite Structural Planes

The simulation results for models with two pre-existing fractures under different filling conditions provide compelling evidence for the crucial role of fracture filling in controlling EDZ development. The progressive reduction in damage extent from model 1 (both fractures unfilled) to model 4 (both fractures filled) demonstrates that filling materials can transform fractures from planes of weakness into elements of internal reinforcement, fundamentally altering the failure mechanisms in fractured rock masses.

The quantitative analysis reveals striking differences in EDZ characteristics across the four models. Model 1, with both fractures unfilled, developed the most extensive damage zone with maximum width (65.2° on the left side, 58.7° on the right), depth (normalized depth l/r = 2.15), and area (512 mm^2). In contrast, model 4, with both fractures filled, exhibited minimal damage with significantly reduced dimensions (width: 41.3° left, 38.9° right; depth: l/r = 1.62; area: 286 mm^2). Models 2 and 3, with partial filling configurations, showed intermediate damage states, with model 3 displaying a more asymmetric damage distribution due to the specific spatial arrangement of the filled fracture. This progressive 44% reduction in the total damage area from model 1 to model 4 underscores the effectiveness of fracture filling in constraining EDZ development.

The primary mechanism through which filling materials enhance stability is the maintenance of rock mass integrity and stress continuity. Stress distribution analysis demonstrates that in model 4, the filling material enables effective stress transmission across fracture planes, maintaining left-wall stresses 15–20% above analytical predictions. This sustained compressive stress state raises the crack initiation threshold and prevents the stress release observed in unfilled models. In models 1–3, significant reductions (35–50%) in the hoop and radial stresses on the fractured left wall indicate substantial stress release through progressive failure, with the unfilled fractures serving as stress relief points where stresses drop to near-zero values.

Furthermore, the filling material physically obstructs crack propagation and coalescence through several mechanisms. In model 1, cracks initiate simultaneously at multiple fracture tips and rapidly coalesce, forming a widespread, interconnected crack network. The unfilled fractures act as preferential paths for crack propagation, leading to the formation of a large, continuous damaged block. In contrast, model 4 exhibits only isolated

microcracks that fail to coalesce into major failure planes, with damage localized to minor spalling at fracture–borewall intersections. The filled fractures in models 2 and 3 reduce damage asymmetry by 42% and 28%, respectively, compared to model 1, confirming that fracture filling promotes more symmetric stress redistribution around excavations.

The crack initiation sequences and propagation paths further illustrate the reinforcing effect of filling materials. In partially filled models, crack initiation preferentially occurs at the tips of unfilled fractures, with filled fractures acting as barriers that deflect crack paths. This barrier effect significantly delays damage progression and prevents the formation of interconnected failure networks. The intermediate states of models 2 and 3 clearly demonstrate that any unfilled fracture segment remains a potential pathway for crack propagation and stress release, highlighting the importance of comprehensive fracture treatment in engineering practice.

From a practical engineering perspective, these results strongly validate grouting and filling techniques as highly effective measures for stabilizing rock masses with multiple structural planes. The demonstrated 44% reduction in damage extent through complete fracture filling provides quantitative support for the efficacy of these techniques. By transforming unfilled fractures into filled ones, the intrinsic strength of the rock mass is enhanced through multiple mechanisms: maintaining stress continuity, increasing fracture strength, and preventing crack coalescence. These findings are particularly relevant for high-level waste disposal repositories and deep-underground energy storage facilities, where long-term stability and minimal rock permeability are paramount. The results also provide critical insights for optimizing grouting strategies in fractured rock masses, suggesting that priority should be given to fractures most likely to initiate damage propagation and those contributing to asymmetric failure patterns.

4.3. Model Verification and Comparative Analysis Based on Actual Rockburst Cases

4.3.1. Jinping "11.28" Rockburst Case with a Single Pre-Existing Fracture

To verify the applicability of the single fracture model in practical engineering, this study selects the Jinping "11.28" rockburst case to conduct numerical simulation and comparative analysis. The mechanical parameters of the granite and filling materials (veins) used in the case study models are identical to those of the other models listed in Table 3. The engineering background of this case involves a pre-existing fault nearly parallel to the tunnel axis with an inclination of approximately 40–50°, providing a typical geological prototype for validating the failure mechanism of fractured rock masses under high in situ stress conditions (Figure 19). By reproducing the rockburst process, the aim is to establish a connection between the simplified model and complex engineering practice.

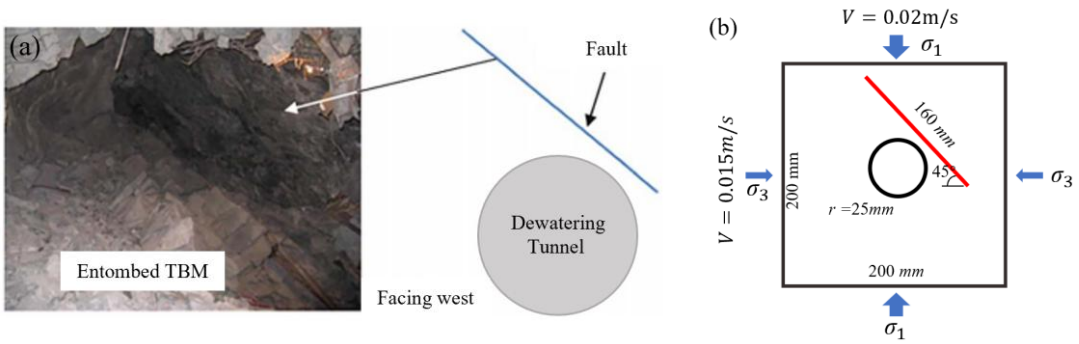

Figure 19. (**a**) Major fault exposed in the Jinping 11.28 rockburst [33]. (**b**) Numerical model diagram of rockburst in Jinping 12.28.

The numerical simulation accurately reproduced the core failure characteristics of the rockburst on site. The V-shaped crack concentration zone formed was highly consistent in morphology and spatial distribution with the 7 m deep V-shaped failure zone measured on site (Figure 20). The crack evolution process (Figure 21a) further indicated that the damage initiated at the end of the fault and gradually extended towards the tunnel wall until it was fully penetrated, which was in line with the actual report's description of all the rock mass below the fault burst. This verified the effectiveness of the discrete element model in simulating the stress-driven fractures' behavior in actual geological structures.

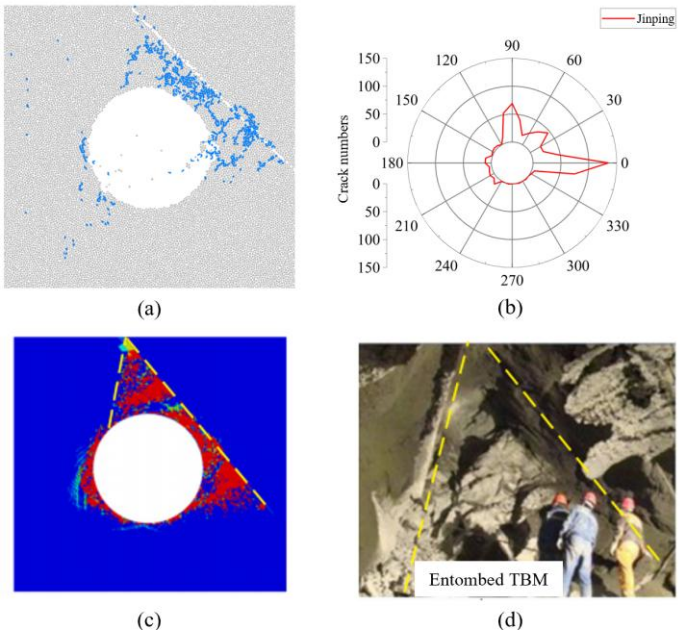

Figure 20. Comparison of rockburst simulation results in Jinping 12.28: (**a**) numerical simulation results, in which the clusters of microcracks in the models are represented by blue dots; (**b**) crack distribution diagram; (**c**) numerical simulation of failure zone comparison, in which the clusters of microcracks in the models are represented by red dots [34]; and (**d**) Jinping 11.28 rockburst site damage area [33].

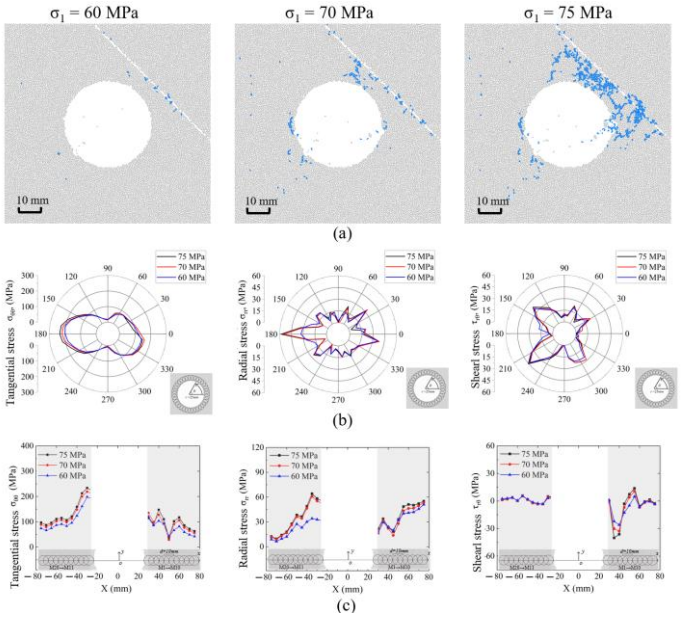

Figure 21. Rockburst simulation results in the Jinping 12.28: (**a**) numerical simulation process, in which the clusters of microcracks in the models are represented by blue dots; (**b**) stress distribution around the tunnel wall; and (**c**) horizontal stress distribution.

The stress distribution characteristics reveal the triggering mechanism of the rockburst (Figure 21b,c). Despite the fault being located above and to the right of the borehole, the failure presents as an asymmetrical V-shaped pit, which is closely related to the stress redistribution. The right wall, being closer to the fault, forms a double stress concentration zone at 350° and 40°, promoting extensive crack propagation, while on the left wall, a more significant radial stress concentration occurs at 180°, with the stress value increasing nearly twice from 60 MPa to 70–75 MPa, leading to local deep fractures. Additionally, the shear stress on the left wall is significantly higher than that on the right wall, and deviates severely from the analytical solution, indicating that the fault has significantly altered the stress distribution pattern around the chamber, thereby inducing asymmetric shear failure. This mechanism reasonably explains why the V-shaped pit on site, although related to the fault location, shows asymmetric development.

This case study provides strong mutual verification with the conclusions of the single fracture model. On the one hand, the 45° dip angle of the fault, as a large, concealed fracture, dominates the development direction and asymmetry of the V-shaped damage zone, further confirming the control of the structural plane's orientation on the geometric shape of the damage zone. On the other hand, the propagation law of cracks initiating from the fault ends is highly consistent with the mechanism of cracks starting from the tip of the fracture in the single fracture model, confirming the universality of the fracture tip as a rupture source. More importantly, this case reveals the intrinsic connection between multi-source stress concentration and complex fracture patterns in a real, high-stress environment, highlighting the significance of validating model research within an actual geological context.

This study, through case verification, demonstrates that the numerical method based on discrete elements can effectively predict the fracture behavior of fractured rock masses under high in situ stress conditions. The occurrence of rockburst is not only controlled by the level of in situ stress, but is more significantly influenced by the location and orientation of structural planes. In engineering practice, sufficient attention should be paid to the concealed fractures around the tunnel, especially near the tunnel wall, as they are prone to become the priority development zones of fractures during the process of stress redistribution. The above understanding provides a theoretical basis for the risk assessment and prevention design of rockburst in deep underground engineering.

4.3.2. One Rockburst Case in Southwest China with Two Pre-Existing Fractures

The second validation case involves a rockburst incident in a deep-buried railway tunnel in Southwest China, characterized by complex geological conditions in a typical alpine valley landscape. With a maximum burial depth of 2080 m, the tunnel passes through Yanshanian granite exhibiting a saturated uniaxial compressive strength of 130–140 MPa and an elastic modulus of 30–60 GPa. Field investigations revealed two dominant structural planes in the section from chainage 194 + 490 to 530, with attitudes of 184°∠50° and 184°∠20°, spaced approximately 2 m apart (Figure 22). These unfilled or partially closed fractures, with widths ranging 0–5 mm, played a crucial role in the rockburst events that occurred during excavation.

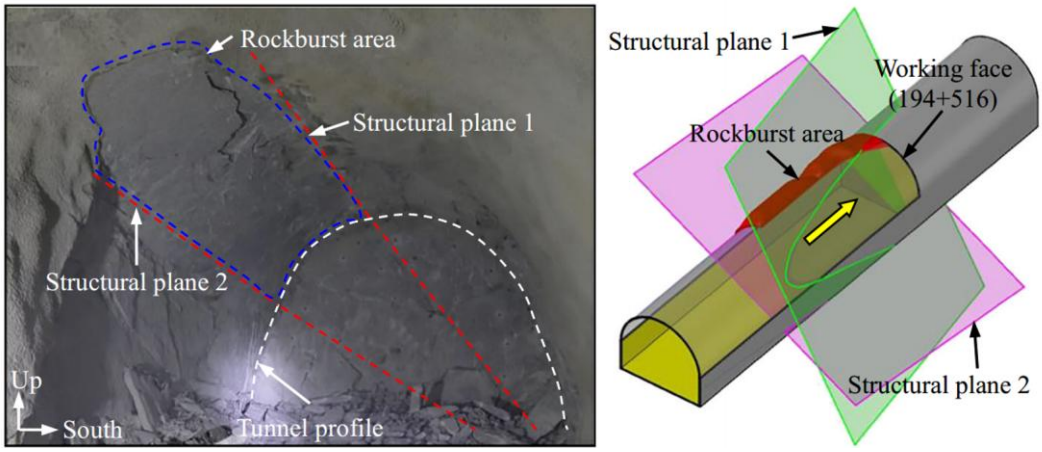

Figure 22. Examples of typical rockbursts that occur in tunnel sections and the related geological conditions [35].

The numerical model successfully replicated the key characteristics observed in the actual rockburst incident. As demonstrated in Figure 23a, the simulation captured the progressive damage evolution under increasing axial stress: the initial crack development along the fracture tips at 60 MPa, followed by their upward and downward extension along Fractures I and II at 80 MPa, and ultimately the formation of an extensive crack network with significant wall spalling at 90 MPa. This damage progression pattern closely matches the field observations of multiple rockburst events ranging from minor to moderate intensity in the tunnel's north arch shoulder to crown area.

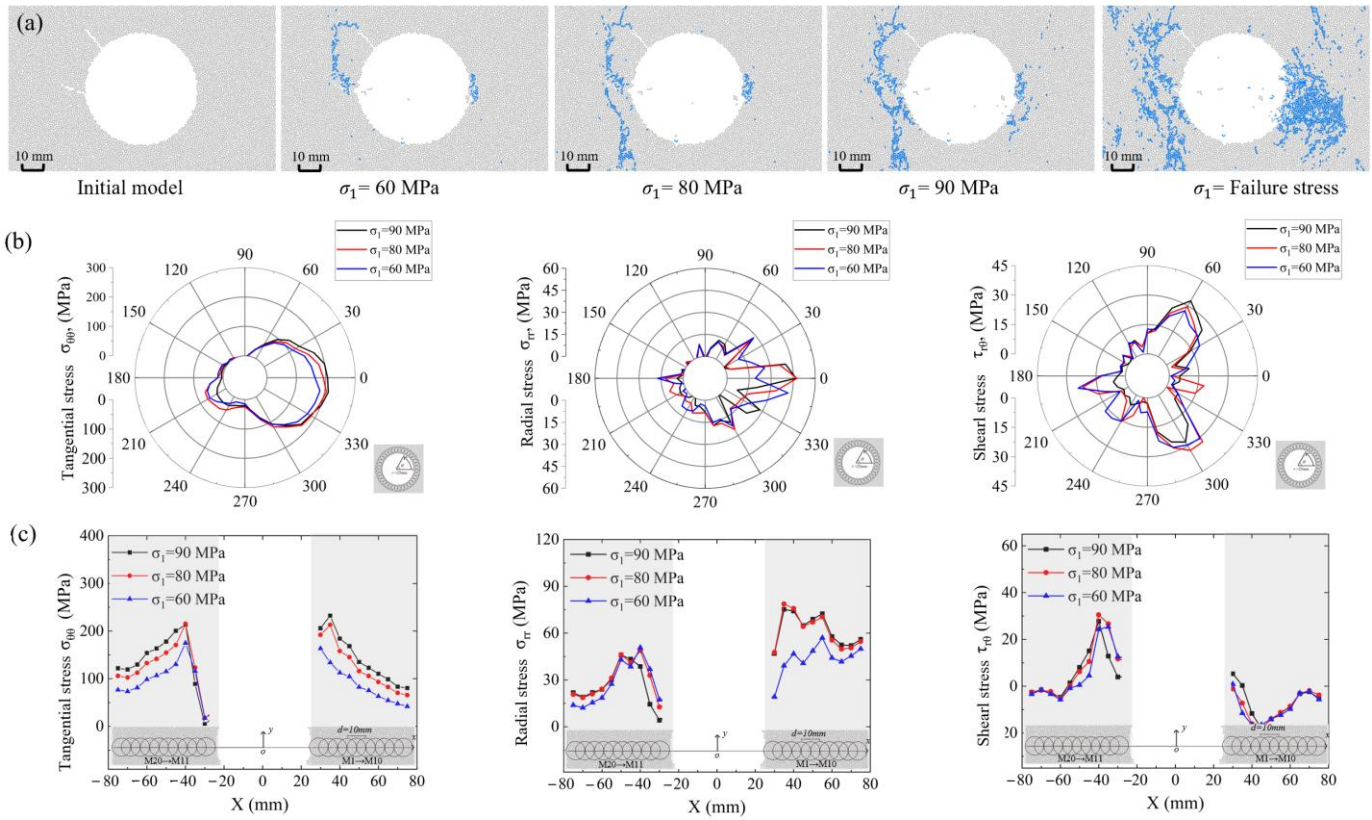

Figure 23. Simulation results of a tunnel in southwest China: (**a**) numerical simulation process, in which the clusters of microcracks in the models are represented by blue dots; (**b**) stress distribution around the tunnel wall; and (**c**) horizontal stress distribution.

Stress distribution analysis provides mechanical validation of the model's reliability. The asymmetric hoop stress distribution around the borehole wall (Figure 23b) accurately reflects the stress redistribution caused by the two fractures, explaining why damage preferentially developed between the structural planes. The migration of radial stress concentration from 10° to 0° with increasing axial stress (Figure 23c) correlates well with the observed rightward crack propagation direction in the actual rockburst. Furthermore, the distinctive shear stress pattern, with a prominent concentration on the left side and sequential stress variation at positions 300° and 60°, convincingly explains the complex crack propagation sequence observed both in simulations and field conditions.

Most significantly, the numerical results demonstrate remarkable consistency with the actual rockburst damage characteristics. As shown in Figure 24, the simulated crack concentration zone between the two fractures aligns perfectly with the actual rockburst pit, measuring 7 × 4 × 1 m^3 (width × height × depth) in dimensions. The bond breakage distribution in the DEM model clearly shows how the fractures initiated from both the fracture tips and eventually coalesced, leading to the detachment of rock blocks, a mechanism that accurately represents the "rock bursting" phenomenon observed in the field.

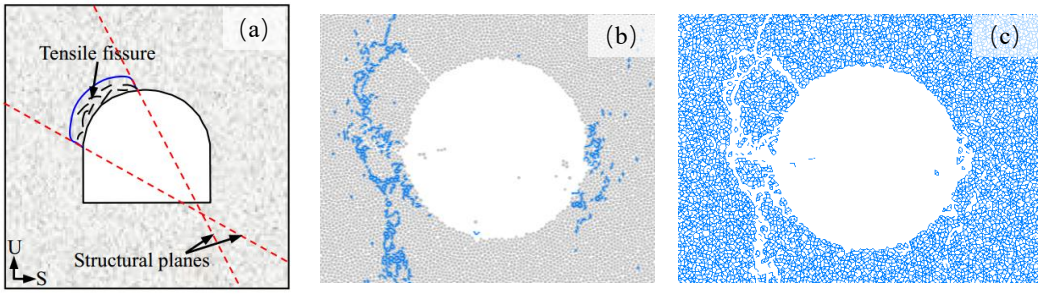

Figure 24. Comparison between simulation results and actual cases: (**a**) schematic diagram of rockburst in a southwest tunnel (Hu et al., 2020) [35]; (**b**) crack distribution diagram of model 1 under the axial stress of 80 MPa, with microcracks represented by blue dots; and (**c**) distribution diagram of bonds of discrete element model.

This successful reproduction of both the damage patterns and stress evolution mechanisms in a real engineering case provides strong validation for the numerical approach adopted in this study. The model's ability to capture the essential physics of rockburst development in fractured rock masses demonstrates its reliability for analyzing similar geotechnical problems. The consistency between simulated and actual rockburst characteristics confirms that the discrete element method with proper parameter calibration can effectively predict excavation-induced damage in complex geological conditions, offering valuable insights for rockburst risk assessment, and can support design in deep tunneling projects through fractured rock masses.

Despite these strengths, it is important to recognize that this study uses a 2D numerical model, which inherently simplifies the true three-dimensional complexity of the system. The plane strain assumption does not fully capture out-of-plane stress effects or the spatial variability of fracture networks—factors that can significantly influence the prediction of excavation damage zone (EDZ) geometry and extent. While the current results provide valuable insights into key mechanical behaviors, future work will focus on developing 3D simulations to enable more rigorous and quantitatively accurate assessments.

5. Conclusions

This study utilizes the discrete element method to elucidate the evolution mechanism of the excavation damage zone (EDZ) in deep-buried tunnels, highlighting the coupled effects of confining pressure and pre-existing structural planes. Key findings are summarized as follows:

(1) Confining pressure exerts a dual influence on EDZ development; it promotes crack initiation and EDZ expansion in intact rock and at exposed fractures by intensifying stress concentration, whereas it suppresses damage around hidden filled fractures through enhanced confinement.
(2) EDZ geometry is primarily governed by fracture orientation, location, and filling condition. Filled fractures maintain stress continuity, raising the crack initiation stress ratio (σ_{ci}/σ_P) to 0.3–0.4 and reducing EDZ area by up to 44% compared to unfilled fractures.
(3) In multi-fractured rock masses, the filling state determines stability. Unfilled fractures facilitate stress release and crack coalescence, while filled fractures act as internal barriers, diverting crack paths and promoting symmetric stress redistribution.
(4) The numerical models accurately reproduced failure patterns from actual rockburst cases, validating the discrete element method as a reliable tool for predicting stress-driven fracture behavior and supporting rockburst risk assessment and support design.

Author Contributions: Conceptualization, Z.L.; methodology, Z.L. and Y.Q.; writing—original draft preparation, Z.L., Y.S. and Y.Q.; methodology, Z.L., Y.Q. and Y.S.; investigation, Z.L., Y.S. and H.D.; model validation, H.D.; project administration, Z.L.; funding acquisition, Z.L.; data curation, Z.L.; conceptualization, Z.L. All authors have read and agreed to the published version of the manuscript.

Funding: This work was funded by the National Science and Technology Major Project for New-type Oil and Gas Exploration and Development (Grant No. 2025ZD1401406).

Data Availability Statement: The data presented in this study are available on request from the corresponding author.

Conflicts of Interest: The authors declare no conflicts of interest. The funders had no role in the design of the study; in the collection, analyses, or interpretation of data; in the writing of the manuscript; or in the decision to publish the results.

References

1. Qian, Q.; Zhou, X. Failure Behaviors and Rock Deformation During Excavation of Underground Cavern Group for Jinping I Hydropower Station. *Rock Mech. Rock Eng*. **2018**, *51*, 2639–2651.
2. Liu, B.; Meng, W.; Zhao, Z.; Lin, T.; Zhang, J. Coupled thermal-hydro-mechanical Modeling on Characteristics of Excavation Damage Zone Around Deep Tunnels Crossing a Major Fault. *Tunn. Undergr. Space Technol*. **2023**, *134*, 105008.
3. Zhu, W.C.; Bruhns, O.T. Simulating Excavation Damaged Zone Around a Circular Opening Under Hydromechanical Conditions. *Int. J. Rock Mech. Min. Sci*. **2008**, *45*, 815–830.
4. Feng, X.; Pei, S.; Jiang, Q.; Zhou, Y.; Li, S.; Yao, Z. Deep Fracturing of the Hard Rock Surrounding a Large Underground Cavern Subjected to High Geostress: In Situ Observation and Mechanism Analysis. *Rock Mech. Rock Eng*. **2017**, *50*, 2155–2175.
5. Gong, F.; Si, X.; Li, X.; Wang, S. Experimental Investigation of Strain Rockburst in Circular Caverns Under Deep Three-Dimensional High-Stress Conditions. *Rock Mech. Rock Eng*. **2019**, *52*, 1459–1474.
6. Lin, H.; Oh, J.; Canbulat, I.; Stacey, T.R. Experimental and Analytical Investigations of the Effect of Hole Size on Borehole Breakout Geometries for Estimation of In Situ Stresses. *Rock Mech. Rock Eng*. **2020**, *53*, 781–798.
7. Lin, H.; Oh, J.; Canbulat, I.; Hebblewhite, B.; Masoumi, H.; Walsh, S. Experimental Study on Borehole Size Effect and Prediction of Breakout Initiation Stress. *Int. J. Rock Mech. Min. Sci*. **2021**, *142*, 104762.
8. Zhou, H.; Meng, F.; Zhang, C.; Hu, D.; Yang, F.; Lu, J. Analysis of Rockhurst Mechanisms Induced by Structural Planes in Deep Tunnels. *Bull. Eng. Geol. Environ*. **2015**, *74*, 1435–1451.

9. Zhang, C.; Feng, X.; Zhou, H.; Qiu, S.L.; Wu, W.P. Rockmass Damage Development Following Two Extremely Intense Rockbursts in Deep Tunnels at Jinping II Hydropower Station, Southwestern China. *Bull. Eng. Geol. Environ*. **2013**, *72*, 237–247.
10. Gu, L.; Feng, X.; Kong, R.; Yang, C.; Han, Q.; Xia, Y. Excavation Stress Path Induced Fracturing Mechanism of Hard Rock in Deep Tunnel. *Rock Mech. Rock Eng*. **2023**, *56*, 1779–1806.
11. Shirole, D.; Walton, G.; Ostrovsky, L.; Masoumi, H.; Hedayat, A. Non-linear Ultrasonic Monitoring of Damage Progression in Disparate Rocks. *Int. J. Rock Mech. Min. Sci*. **2018**, *111*, 33–44.
12. Zhao, Z.; Guo, T.; Li, S.; Wu, W.; Yang, Q.; Chen, S. Effects of Joint Surface Roughness and Orientational Anisotropy on Characteristics of Excavation Damage Zone in Jointed Rocks. *Int. J. Rock Mech. Min. Sci*. **2020**, *128*, 104265.
13. Lei, Q.; Latham, J.; Xiang, J.; Tsang, C.-F. Role of Natural Fractures in Damage Evolution around Tunnel Excavation in Fractured Rocks. *Eng. Geol.* **2017**, *231*, 100–113.
14. Indraratna, B.; Oliveira, D.A.F.; Brown, E.T.; de Assis, A.P. Effect of Soil–Infilled Joints on the Stability of Rock Wedges Formed in a Tunnel Roof. *Int. J. Rock Mech. Min. Sci*. **2010**, *47*, 739–751.
15. Indraratna, B.; Premadasa, W.; Brown, E.T.; Gens, A.; Heitor, A. Shear Strength of Rock Joints Influenced by Compacted Infill. *Int. J. Rock Mech. Min. Sci*. **2014**, *70*, 296–307.83.
16. Duan, K.; Kwok, C.Y. Evolution of Stress-Induced Borehole Breakout in Inherently Anisotropic Rock: Insights from Discrete Element Modeling. *J. Geophys. Res. Solid Earth* **2016**, *121*, 2361–2381.
17. Xiang, Z.; Moon, T.; Si, G.; Oh, J.; Canbulat, I. Numerical Analysis of V-Shaped Borehole Breakout Using Three-Dimensional Discrete-Element Method. *Rock Mech. Rock Eng*. **2023**, *56*, 3197–3214.
18. Hao, X.; Feng, X.; Yang, C.; Jiang, Q.; Li, S.-J. Analysis of EDZ Development of Columnar Jointed Rock Mass in the Baihetan Diversion Tunnel. *Rock Mech. Rock Eng*. **2016**, *49*, 1289–1312.
19. He, C.; Mishra, B.; Shi, Q.; Zhao, Y.; Lin, D.; Wang, X. Correlations Between Mineral Composition and Mechanical Properties of Granite Using Digital Image Processing and Discrete Element Method. *Int. J. Min. Sci. Technol*. **2023**, *33*, 949–962.
20. Zhao, Z.; Suo, Y.; Liu, Z.; Zhao, X.; Liu, B.; Zhao, Y.; Zhang, S. Effect of Pre-existing Infilled Fracture on Characteristics of Failure Zones around Circular Opening. *Comput. Geotech*. **2024**, *169*, 106228.
21. Su, G.; Yan, X.; Zheng, Z.; Li, C.; Zhao, X.; Ren, H. Experimental Study on the Influence of a Small-Scale Single Structural Plane on Rockburst in Deep Tunnels. *Rock Mech. Rock Eng*. **2023**, *56*, 669–701.
22. Yuan, P.; Zhang, Q.; Li, A. Numerical Analysis of Cyclic Impact Damage Evolution of Rock Materials under Confining Pressure. *Appl. Sci*. **2023**, *13*, 8822.
23. Ma, B.; Ding, X.; Chen, X. Reloading Mechanical Properties and Particle Flow Simulation of Pre-Peak Confining Pressure Unloading Sandstone. *Appl. Sci.* **2023**, *13*, 5775.
24. Yin, P.; Yang, S.; Gao, F.; Tian, W. Experimental and DEM Simulation Study on the Mechanical Characteristic and Strain Energy Evolution of Longmaxi Shale under a Confining Pressure Unloading Path. *Energies* **2023**, *16*, 5960.
25. Jiang, R.; Dai, F.; Liu, Y.; Li, A. Fast Marching Method for Microseismic Source Location in Cavern-Containing Rockmass: Performance Analysis and Engineering Application. *Engineering* **2021**, *7*, 1023–1034.
26. Li, A.; Liu, Y.; Dai, F.; Liu, K.; Wei, M. Continuum Analysis of the Structurally Controlled Displacements for Large-scale Underground Caverns in Bedded Rock Masses. *Tunn. Undergr. Space Technol*. **2020**, *97*, 103288.
27. Zhang, Y.; Su, G.; Li, Y.; Wei, M.; Liu, B. Displacement Back-Analysis of Rock Mass Parameters for Underground Caverns Using a Novel intelligent Optimization Method. *Int. J. Geomech*. **2020**, *20*, 04020035.
28. Potyondy, D.O.; Cundall, P.A. A Bonded-particle Model for Rock. *Int. J. Rock Mech. Min. Sci*. **2004**, *41*, 1329–1364.
29. Potyondy, D.O. The Bonded-Particle Model as a Tool for Rock Mechanics Research and Application: Current Trends and Future Directions. *Geosyst. Eng*. **2015**, *18*, 1–28.
30. Dean, W.R. Mathematical Theory of Elasticity. By I. S. Sokolnikoff, Second Edition. Pp. Xi, 476, $9.50. 1956. (McGraw-Hill). *Math. Gaz.* **1959**, *43*, 61–62.
31. Hazzard, J.F.; Young, R.P. Simulating Acoustic Emissions in Bonded-Particle Models of Rock. *Int. J. Rock Mech. Min. Sci*. **2000**, *37*, 867–872.
32. Cai, M.; Kaiser, P.K. In-situ Rock Spalling Strength near Excavation Boundaries. *Rock Mech. Rock Eng*. **2014**, *47*, 659–675.
33. Zhang, C.; Feng, X.; Zhou, H.; Qiu, S.L.; Wu, W.P. Case Histories of Four Extremely Intense Rockbursts in Deep Tunnels. *Rock Mech. Rock Eng*. **2012**, *45*, 275–288.

34. Manouchehrian, A.; Cai, M. Numerical Modeling of Rockburst Near Fault Zones in Deep Tunnels. *Tunn. Undergr. Space Technol.* **2018**, *80*, 164–180.
35. Hu, L.; Feng, X.; Xiao, Y.; Wang, R.; Feng, G.-L.; Yao, Z.-B.; Niu, W.-J.; Zhang, W. Effects of Structural Planes on Rockburst Position with Respect to Tunnel Cross-Sections: A Case Study Involving a Railway Tunnel in China. *Bull. Eng. Geol. Environ.* **2020**, *79*, 1061–1081.